MATERIALS SCIENCE

In situ structural-functional synchronous dissection of dynamic neuromuscular system via an integrated multimodal wearable patch

Hang Zhao[1,2,3]†, Weicen Chen[2]†, Yuanheng Li[1,4]†, Hailiang Wang[5], Hanfei Li[1,6], Tengfei Li[1,6], Fei Han[1], Jing Sun[1], Laixin Huang[7], Xinhao Peng[1,3], Jianzhong Chen[2], Yihang Yang[1], Xin Qiu[8], Yan Liu[1], Huan Yu[1], Wen Hou[1], Qingsong Li[1], Guibing Fu[8], Chao You[8], Xijian Liu[9], Fei Li[7], Xiangxin Li[1], Guoru Zhao[1], Lin Wang[1], Peng Fang[1], Guanglin Li[1], Hairong Zheng[2], Meifang Zhu[5], Wei Yan[5]*, Qiong Tian[1]*, Teng Ma[2,10]*, Zhiyuan Liu[1,10,11]*

Neuromuscular abnormality is the leading cause of disability in adults. Understanding the complex interplay between muscle structure and function is crucial for effective treatment and rehabilitation. However, the substantial deformation of muscles during movement (up to 40%) poses challenges for accurate assessment. To address this, we developed a wearable structural-functional sensing patch (WSFP) that enables synchronous analysis of muscle structure and function. The WSFP incorporates a soft, stretchable electrode array for high-performance electrophysiological monitoring with low contact impedance and high stability. Its innovative design absorbs skin deformation stress, ensuring stable adhesion of a flexible ultrasound transducer array, offering higher-fidelity imaging. With dynamic tissue imaging, it allows real-time visualization of muscle structure. The WSFP achieves superior accuracy in dynamic action recognition and disease assessment compared to single-modal methods, maintaining stable operation during motion for up to 72 hours. This study advances neuromuscular system analysis and improves diagnostic precision.

INTRODUCTION

Neuromuscular diseases (NMDs) are a diverse group of conditions caused by defects in peripheral neurons (e.g., neuropathies, amyotrophic lateral sclerosis, and stroke), muscles [congenital muscular torticollis (CMT) and myopathies], and neuromuscular junctions (myasthenic syndromes) (*1*, *2*). Despite the various pathogenesis, they share some common features, e.g., muscle weakness, twitching, torpidity, and cramps, leading to mobility impairments, pararthria, and self-caring problems (*3*, *4*). For example, neuromuscular problems induced by stroke are the leading cause of disability in adults and the second most common cause of death, leading a rate of 11.8% worldwide and more than 110 million of the global disability (*5*). Amyotrophic lateral sclerosis, which is a rare but fatal peripheral neurodegenerative disease, can be difficult to recognize in the early stages (*6*). CMT is another disease that manifests muscle structural and functional changes of the sternocleidomastoid (SCM) muscle in the developmental stages of children with a reported incidence of 0.3 to 2% (*7*, *8*). This condition can have a lasting negative impact on a child's posture, neck function, and quality of life. All those NMDs require effective sensing technology to achieve early diagnosis, evaluation, and related therapy (*9*, *10*).

Biosignals from the neuromuscular system are mainly divided into two types (*11*): One is structural signals, e.g., imaging modalities such as ultrasound and magnetic resonance imaging; another is functional signals, such as electrophysiology (EP), chemicals, and so forth. Previously, for individual detection of those two kinds of signals, people proposed various methods to optimize the flexibility, sensitivity, and channel numbers of the sensing system (*12*–*14*). For ultrasound imaging, commercial ultrasound devices are rigid and in large size, making them unsuitable for long-term continuous and stable monitoring (*15*–*18*). Typically, individuals must hold these rigid ultrasound devices and apply pressure to ensure good contact with the skin for clear tissue imaging. While it may work well for deep tissue imaging, applying pressure can lead to muscle deformation, compromising the accurate reflection of the true structural characteristics, especially in muscle imaging. Consequently, there has been considerable focus on developing flexible and stretchable ultrasound probes to replace conventional rigid ones for blood pressure, blood flow detection, and structural imaging (*19*–*22*). For EP monitoring, there is a focus on achieving high conformity of the interface electrodes with the skin by making them softer, stretchable, and air permeable (*23*–*26*). These efforts have benefited the elimination of motion artifacts caused by skin deformation during dynamic movements of the human body. Furthermore, advancements in bioinspired three-dimensional architected electronic skins with decoupled unparalleled sensing capabilities demonstrate potential for developing complex, flexible sensing systems. These systems mimic the spatial distribution of mechanoreceptors in human skin, further enhancing the accuracy and

[1]Neural Engineering Centre, Shenzhen Institutes of Advanced Technology, Chinese Academy of Sciences, Shenzhen 518055, China. [2]Institute of Scientific Instrumentation, Shenzhen Institutes of Advanced Technology, Chinese Academy of Sciences, Shenzhen 518055, China. [3]University of Chinese Academy of Sciences, Beijing 101408, China. [4]Department of Mechanical, Materials and Manufacturing Engineering, University of Nottingham Ningbo China, Ningbo 315100, China. [5]State Key Laboratory for Modification of Chemical Fibers and Polymer Materials, College of Materials Science and Engineering, Donghua University, Shanghai 201620, China. [6]School of Mechanical, Electrical and Information Engineering, Shandong University, Weihai 264209, China. [7]Shenzhen Institutes of Advanced Technology, and Key Laboratory of Biomedical Imaging Science and System, Chinese Academy of Sciences, Shenzhen 518055, China. [8]Shenzhen Children's Hospital of Shantou Medical University, Shenzhen 518048, China. [9]College of Chemical and Chemical Engineering, Shanghai University of Engineering Science, Shanghai 201620, China. [10]National Innovation Center for Advanced Medical Devices, Shenzhen 518100, China. [11]Key Laboratory of Biomedical Imaging Science and System, Chinese Academy of Sciences, Shenzhen 518055, China.
*Corresponding author. Email: zy.liu1@siat.ac.cn (Z.L.); teng.ma@siat.ac.cn (T.M.); qiong.tian@siat.ac.cn (Q.T.); weiyan@dhu.edu.cn (W.Y.)
†These authors contributed equally to this work.

functionality of wearable sensors (*27*). However, it should be noted that evaluation solely by monitoring structural or functional aspects often leads to incomplete data and may result in misdiagnosis. For example, CMT is a disease related to muscle fibrosis. In the early stage, it is hard to observe it using ultrasound but can be detected using electromyography (EMG) (*28*). Subsequently, ultrasound imaging can provide further details on muscle fibrosis, such as thickness and depth (*29*, *30*). Therefore, it is highly necessary to achieve in situ structural-functional biosignals detection and to elucidate their interplay to fully understand the working process of neuromuscular system (*31*). However, the notable deformation strain experienced by the muscular system has resulted in a noticeable absence of a framework for a flexible sensing system designed specifically for this purpose. An in situ dual-modal sensing system is in high demand, especially one capable of achieving in situ long-term dissection of both structural and functional information, along with their correlation. Such a system would empower researchers to track the diseases progress or conditions over time, facilitating a more comprehensive understanding of the NMD and contributing to early diagnosis and the formulation of improved treatment plans.

Here, we report a framework of a wearable structural-functional sensing patch (WSFP) via integrating a flexible ultrasound transducer (FUT) array and soft stretchable electrodes. It can achieve in situ synchronous dissection of structural (ultrasound imaging) and functional information (EMG) of peripheral muscles. Comprising 128 lead zirconate titanate (PZT) elements with a spacing of 0.3 mm between elements, the WSFP features a frequency of 7.5 MHz and a bandwidth of 65%. It demonstrates low acoustic impedance and minimal interelement cross-talk, offering ultrasound imaging of similar quality to that of traditional rigid arrays. Acting as stress-relief (SR) layers, the soft stretchable electrodes release stress generated during 30% skin deformation on the back and neck, enabling stable and clear ultrasound imaging with improved quality over current flexible patches during dynamic skin deformation processes. The dual-modal synchronous dissection of WSFP is validated in both normal subjects and patients. The WSFP is attached to the forearm brachioradialis, back erector spinae, and neck SCM muscles to dissect both muscle ultrasound imaging and EMG signals. A clear negative correlation is observed between decreased muscle thickness and increased root mean square (RMS) of EMG signal during muscle contraction. Data analysis reveals higher action recognition accuracy in dual-modal data compared to mono-modal data. For children with CMT, WSFP demonstrates higher screening accuracy compared to mono-modal data of muscle ultrasound imaging or EMG. Besides, we demonstrate that WSFP enables 72-hour wearing and achieves the desired structural-functional monitoring during motion. Compared to other studies, WSFP achieves stable dual-mode monitoring under 37.5% skin deformation and maintains imaging stability for over 150 head rotations. In addition, during the monitoring process, the WSFP does not cause tissue deformation, thereby reflecting the real structure of the muscle (table S1). This in situ structural-functional flexible sensing patch opens up the synchronous dissection of tissue structure and function. It holds great potential for precise neuromuscular diagnosis, smart treatment, and rehabilitation.

RESULTS

Design and overview of the structural-functional flexible sensing patch

The WSFP, with a total thickness of ~4.5 mm, features the synchronous dissection of functional and structural information of tissues by attaching it directly on targeted human skin (Fig. 1A). It is flexible (Fig. 1B, i) with an array of soft and stretchable electrodes acting as the SR layer on top of the FUT (Fig. 1B, ii and iii). The SR layer with an overall thickness of 2 mm, including an Ecoflex encapsulation layer, exhibits remarkable stretchability as large as 500% (fig. S1), serving as the dual purpose of collecting 10-channel EMG signals and releasing the stress from the deformed skin to FUT. The electrodes consist of 10 channels, with a 1-cm spacing between monitoring points (fig. S2). The FUT imaging component, with a total thickness of ~2.5 mm, which is attached on the opposite side of the EMG electrodes, consists of piezoceramic-based PZT arrays mounted on a flexible printed circuit board (FPCB). The fabrication process is illustrated in fig. S3. This arrangement forms a flexible acoustic stack, complemented by a 2-mm alumina silicone rubber [polydimethylsiloxane (PDMS)] backing layer (Fig. 1B, iv). The FUT consists of 128 PZT, designed with a center frequency of 7.5 MHz and a bandwidth of 65%. Thanks to the incorporation of a SR layer, the device not only facilitates functional monitoring in conjunction with structural imaging but also ensures conformal adhesion to the skin, even when the skin is deformed during certain actions of torsion or stretching. The good adhesion of WSFP to the skin relies on a stretchable water-based polyacrylate pressure-sensitive adhesive (provided by Desai Chemical Trade Co. Ltd., Jiangming). The interfacial toughness of adhesive with the skin reached 30 J/m^2 (*32*).

During dynamic movements, such as fist clenching and bending, the device maintains good adhesion to the skin of the forearm and back despite the great strain of surface skin of 7.2 and 26.8%, respectively (figs. S4 to S5). Notably, during head rotation, where the skin deformation reaches 37.5%, consistent with reported data (*33*), the device, affixed to the neck skin, consistently upholds a secure adhesion state (Fig. 1C). Strikingly, WSFP demonstrates the capability to consistently and reliably monitor muscle structural changes, even under notable skin surface strain (Fig. 1D). Even more pleasantly, the FUT with a 2-mm SR layer remains conformal adhesion with skin after 150 rotations of the neck, while the FUT without the SR layer detaches from the skin after six rotations of the neck (Fig. 1E). It enables more accurate and reliable tissue visualization without compromising the integrity of the tissue structure, thereby greatly enhancing the quality of diagnostic imaging. This adhesion state persists reliably throughout the entire 72-hour wearable period, enabling subjects to participate in various activities, including work, exercise, eating, and sleeping. Traditional commercial ultrasound imaging (7.5 MHz; Siemens Acuson L10-5 Ultrasound Transducer) requires considerable pressure to achieve clear tissue imaging, even in the presence of the coupling agent (Fig. 1F, i, and movie S1). In contrast, WSFP achieves tissue imaging by directly attaching to the skin (Fig. 1F, ii). For traditional commercial ultrasound imaging, applied pressure can cause tissue deformation of 21.1%, especially affecting the superficial tissues like muscles, which fails to reflect the true structural characteristics of the tissue (Fig. 1G). Compared to traditional EMG electrodes and ultrasound probes, the WSFP exhibits superior stretchability, low contact impedance, and high sensitivity. The WSFP offers comfortable wearability, allowing for continuous use for up to 72 hours (table S2). Furthermore, in comparison to other ultrasound probes documented in the literature (*19*–*22*, *34*–*40*), our WSFP stands out due to its structural-functional sensing capabilities (fig. S6 and table S3).

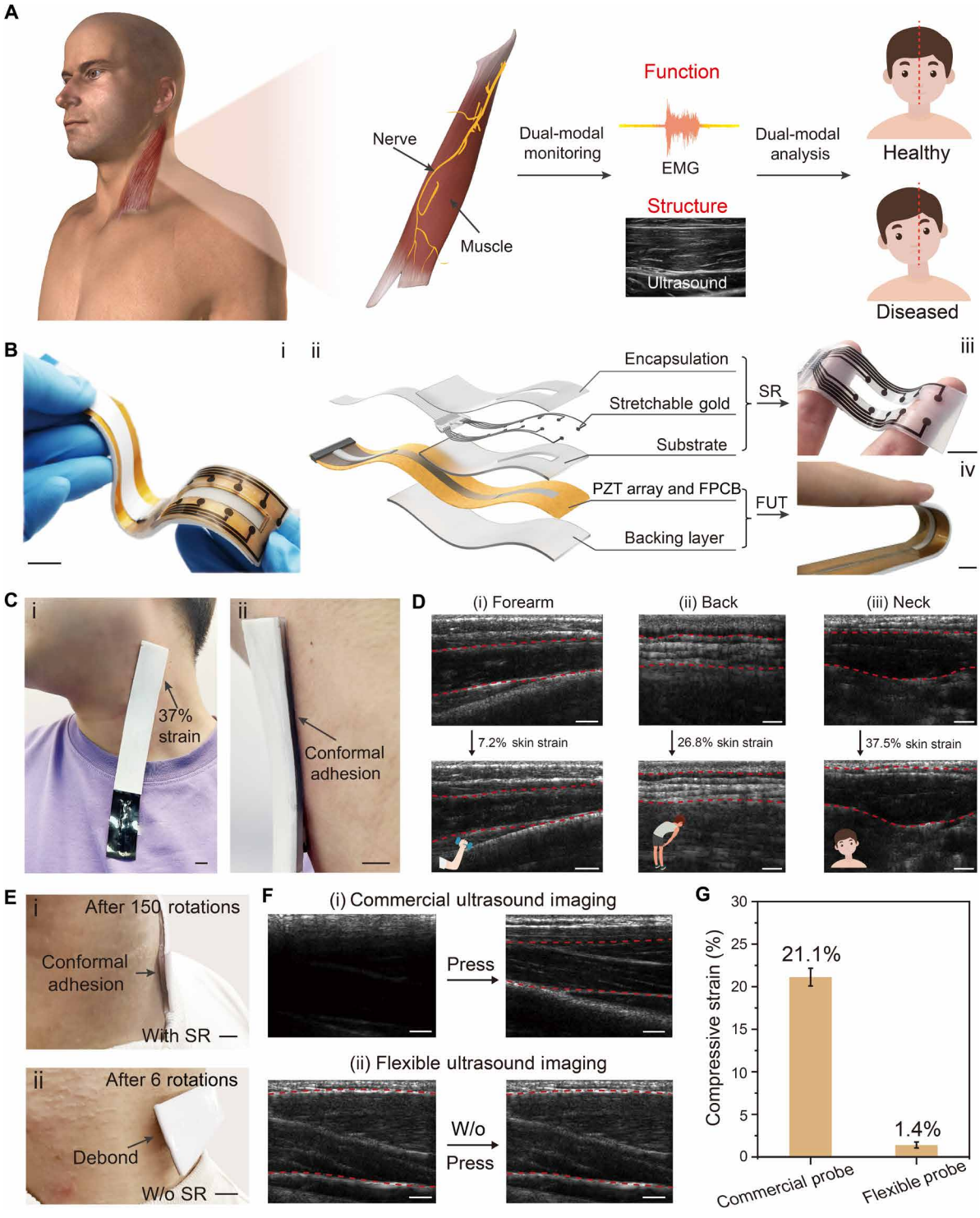

Fig. 1. Overview of the wearable integrated structural-functional sensing patch for in situ synchronous monitoring of muscular ultrasound imaging and functional signals. (**A**) Pictures to demonstrate one of the targeted muscles: SCM muscles that can deform largely with mechanical strain of ~30% in skin. The structural-functional sensing will benefit the precise diagnoses, e.g., muscle fibrosis and disorders. (**B**) Images of the integrated (i) and layered (ii) WSFP, as well as images of separate the SR layer (iii) and the FUT (iv). Scale bars, 1 cm. (**C**) Images depicting the conformable attachment of WSFP on neck. Scale bars, 1 cm. (**D**) Ultrasound imaging of the brachioradialis, erector spinae, and SCM muscles was performed at multiple instances when the skin surface strain of the forearm, back, and neck monitored by WSFP reached 7.2, 26.8, and 37.5%, respectively. Scale bars, 5 mm. (**E**) Attachment states of the FUT with a 2-mm SR layer after 150 rotations of the neck (i) and without a SR layer after 6 rotations of the neck (ii). Scale bars, 1 cm. (**F**) Commercial rigid ultrasound probe is used for muscle structural imaging, and pressure is required causing structure change to the muscle (i), which indicates that the commercial ultrasound probe could not reflect the real structure of the muscle, and FUT is used for muscle structural imaging without pressure required and muscle thickness appears notably larger than that captured by the commercial probe (ii). Scale bars, 5 mm. (**G**) Commercial ultrasound probes cause 21.1% tissue deformation during compression imaging, whereas flexible ultrasound probes induce only 1.4% tissue deformation when attached directly for imaging.

Conformal and stable adhesion of WSFP with skin

This version of WSFP enables imaging without the requirement of pressure, and it still faces challenges in achieving stable ultrasound imaging during dynamic skin deformation. FUT is flexible but lacks inherent softness and stretchability, causing it to detach easily from the skin when the skin is stretched during certain movements (*34*, *38*). To address this issue, a proposed solution is to introduce a laminated SR layer between the skin and the FUT. This additional layer can absorb the stress that occurs when the skin is stretched, preventing it from inducing large shear stress between the FUT and skin, and the further detachment (Fig. 2A).

Here, the SR layer needs to be soft and stretchable to conform to the skin, ensuring close contact and minimizing air gaps. This allows the layer to absorb and distribute stress effectively, maintaining stable ultrasound imaging during skin deformation. Ecoflex, with a modulus of only 0.15 MPa and a stretchability of up to 1000%, proves to be an ideal material for this purpose due to its soft and elastic properties (fig. S7). To optimize the thickness of the SR layer, finite element modeling is used to calculate the shear stress at the interface between the Ecoflex SR layer and the skin (Fig. 2B). When the skin is subjected to a 30% strain, it is observed that the 2-mm–thick SR layer withstands a shear stress of 16 kPa (Fig. 2B). In contrast, the 0.5-mm–thick SR layer has to endure a shear stress of 27 kPa (fig. S8), approximately 1.7-fold increase compared to that of the 2 mm in thickness, indicating the high risk in detachment of FUT. We further investigate the effect of materials by using other elastic polymers, such as PDMS and styrene-ethylene-butadiene-styrene (SEBS). It is observed that the performance achieved using Ecoflex is superior, primarily attributed to its lower modulus compared to that of PDMS (Fig. 2C and fig. S9) and SEBS (Fig. 2D and fig. S10).

We then study the imaging effects of Ecoflex SR layers with varying thickness on different muscles during real-time dynamic processes. First, we attach FUT integrated with Ecoflex SR layers to the SCM muscle on the neck (fig. S11). It demonstrates that the FUT equipped with the SR layer outperforms the one without it in imaging quality. Specifically, during right rotations, the FUT without a SR layer similarly experiences imaging failure. Areas of failure still exist in the ultrasound imaging with 0.5- and 1-mm SR layers. In contrast, the FUT integrated with the 2-mm Ecoflex SR layer maintains stable and clear imaging during three consecutive right rotations in the neck (Fig. 2E). After several right rotations, the flexible probe without a SR layer completely detaches from the skin, whereas the FUT integrated with the 2-mm Ecoflex SR layer remains closely adhere to the skin (Fig. 2F). During left rotations and left-right flexions, the presence of a 2-mm SR layer enables stable ultrasound imaging of the SCM muscle, contrasting with the imaging quality in the absence of SR layers or the use of other thicknesses (figs. S12 to S14). Moreover, the FUT integrated with the 2-mm Ecoflex SR layer consistently maintains stable ultrasound imaging even during approximately 150 left and right rotations. This allows for clear visualization of the structure of the SCM muscle throughout the movement (fig. S15 and movie S2), achieving improved quality compared to other methods (*20*). In contrast, the standalone FUT experiences a direct imaging failure during right rotations (movie S3). In addition, for FUTs with varying thicknesses of PDMS and SEBS attached to the neck, the number of rotations each could withstand increased with thickness. Specifically, 2-mm PDMS endured only 15 rotations, while 2-mm SEBS managed just eight rotations (fig. S16), both considerably lower than the 150 rotations sustained by 2-mm Ecoflex. These results further support the choice of 2-mm Ecoflex as the SR layer.

Except for the neck muscles, the muscles on the back undergo even greater stretching during movements such as stooping down. We then proceed to assess the dynamic imaging effects by affixing FUT integrated with Ecoflex SR layers of different thicknesses to the erector spinae muscles on the back. By varying the thickness of the SR layer, our objective is to assess the influence of layer thickness on the stability and quality of ultrasound imaging during movements involving the back. Ultrasound imaging under different gestures, including stooping down and twisting of the waist, are examined. In short, we could observe the similar results with that of neck muscles (Fig. 2, G to H, and figs. S17 to S18). Therefore, the 2-mm Ecoflex SR layer provides consistent stability and clarity in imaging during all types of motions. Building upon these findings, we have identified the 2-mm–thick Ecoflex as the optimal SR layer for further research and development.

The collected data highlight the effectiveness of different thickness of SR layers in enhancing ultrasound imaging performance during dynamic movements. Specifically, we observe that the WSFP integrated with a 2-mm Ecoflex SR layer maintains stable and clear imaging even under large deformations of up to 40%. This contrasts with the imaging failure areas seen with WSFP without an SR layer or with thinner SR layers (0.5 and 1 mm), particularly during movements that induce substantial skin strain. These results are visually evident from the dynamic ultrasound imaging performed on various body parts, including the neck and back, as shown in Fig. 2 (E to H) and supporting figures (figs. S12 to S18). The superior imaging stability offered by the 2-mm Ecoflex SR layer demonstrates its necessity for ensuring reliable ultrasound imaging during dynamic monitoring.

Furthermore, we compare a commercial ultrasound probe, a FUT without the SR layer, and a FUT with a 2-mm SR layer. In all cases, an ultrasound coupling agent is applied to the PZT array section, and imaging is performed on a phantom. Because the SR layer is not attached to the PZT array used for ultrasound imaging, it does not produce artifacts. The imaging results show a slight reduction in brightness and contrast for the FUT with the 2-mm SR layer compared to the FUT without it (fig. S19). This reduction is likely due to some ultrasound energy attenuation caused by the extra 2 mm of coupling gel, rather than the SR layer itself. Therefore, we conclude that the SR layer does not introduce notable artifacts.

Performance of FUT and soft electrodes in WSFP

Before stepping into the dual-modal functional and structural dissection, we characterize the detailed properties of the FUT and the soft electrode for the respective ultrasound imaging and EP monitoring. The resonant frequency, mechanical coupling efficiency, energy transmission efficiency, and impedance analysis of FUT are analyzed, which are summarized Fig. 3 (A to E). The stretchability, contact impedance, and cycling performance of the stretchable electrode are shown in Fig. 3 (F to H).

Simulations using PiezoCAD software is conducted to predict the acoustic performance of the FUT, and the results closely aligned with the experimental data, demonstrating the FUT's high performance. The simulated resonant frequency is approximately 6.4 MHz, with an impedance of 67.6 ohm (fig. S20A). In comparison, the measured resonant frequency is 6.35 MHz, with an impedance of 39.5 ohm (Fig. 3A), with the discrepancy potentially stemming

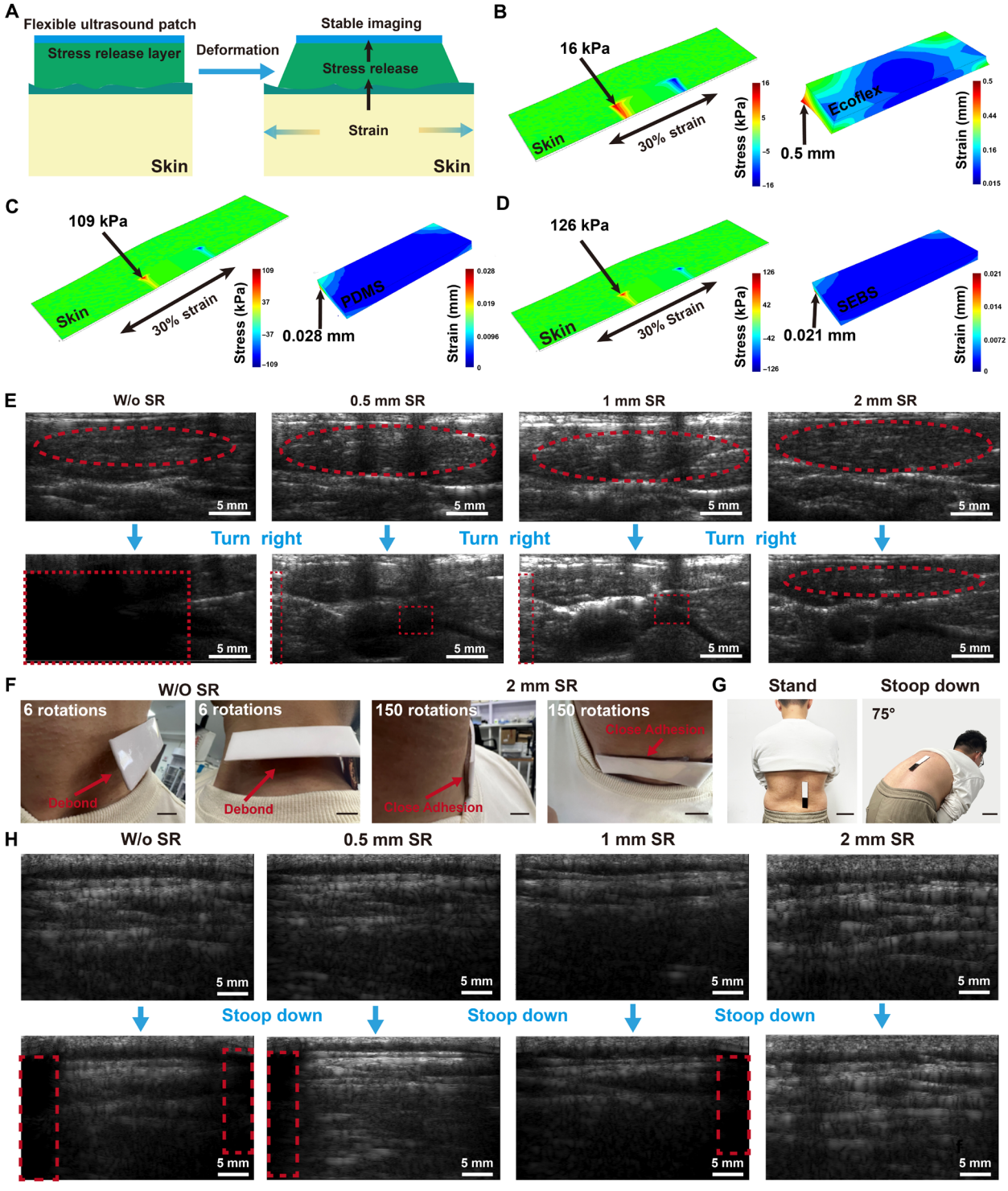

Fig. 2. Advance of the ultrasound imaging via WSFP and the contribution of SR layer to the imaging and wearability. (**A**) Illustration pictures to show the contribution mechanism of SR layer to the stable adhesion of WSFP to skin. (**B**) Finite element modeling is used to calculate the shear stress and deformation experienced by the 2-mm–thickness Ecoflex SR layer with a skin deformation of 30%. Finite element modeling is used to calculate the shear stress and deformation experienced by the 2-mm–thickness (**C**) PDMS and (**D**) SEBS with a skin deformation of 30%. (**E**) Ultrasound imaging of the neck muscles without and with a 0.5-, 1-, and 2-mm Ecoflex SR layer during right rotation. (**F**) Photos of the ultrasound probe attached to the neck skin with and without a SR layer after several right rotations of head. Scale bars, 1 cm. (**G**) Photos of the FUT attached to the back muscles of the subjects while standing and stooping down with 75°. Scale bars, 1 cm. (**H**) The ultrasound imaging of the back muscles without a SR layer and with 0.5-, 1-, and 2-mm Ecoflex SR layers during stoop down. The red dotted squares are the areas of failure imaging.

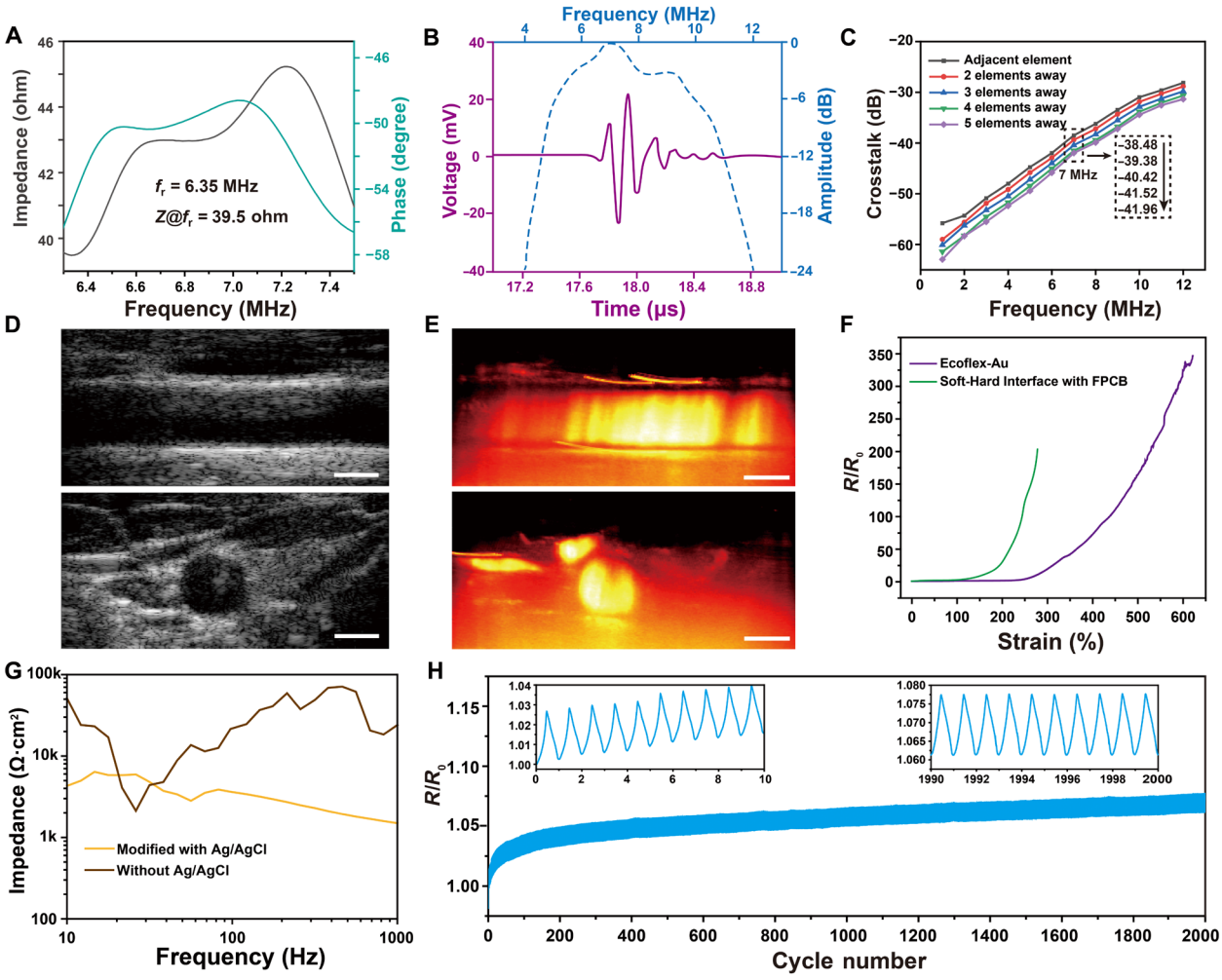

Fig. 3. Performance of FUT and soft electrodes in WSFP. (**A**) Electrical impedance spectrum with the amplitude and phase angle of FUT. (**B**) Pulse-echo response and frequency spectrum of FUT. (**C**) Cross-talk check of neighboring PZT elements. (**D**) Cervical aorta images using FUT. (**E**) Functional Doppler images of cervical aorta using FUT. (**F**) Stretchability of the stretchable electrodes (also used as SR layer) and the soft-hard interface. (**G**) Contact impedance of skin-electrodes modified with Ag/AgCl and without Ag/AgCl modification. (**H**) Resistance changes of stretchable electrodes, also used as SR layer at 100% strain for 2000 cycles. The inserts are resistance changes of the first and last 10 cycles.

from fabrication-related factors. In addition, the simulated pulse-echo response and frequency spectrum indicate a center frequency of around 7.1 MHz and a −6-dB bandwidth of approximately 83.1% (fig. S20B). The experimental results show a measured center frequency of 7.5 MHz and a −6-dB bandwidth of 65% (Fig. 3B). The difference in center frequency and bandwidth between the simulation and measurement is likely due to the fabrication-related factors such as variations in thickness control.

Furthermore, acoustic-electric cross-talk, which signifies the extent of reciprocal impact between the mechanical and electrical characteristics of the FUT, is evaluated. It encompasses alterations in the electrical signal resulting from the transducer's mechanical movement and the mechanical motion triggered by the electrical signal, thereby directly influencing the precision and lucidity of ultrasound imaging. In the five consecutive adjacent elements shown in Fig. 3C, the measured cross-talk levels are −38.48, −39.38, −40.42, −41.52, and − 41.96 dB, respectively. These values meet the requirements for linear array configuration in ultrasound imaging (*41*). The designed FUT not only has the characteristics of high frequency and high bandwidth but also exhibits outstanding imaging capabilities. Besides being used for muscle structural imaging, it can also be used for structural and functional Doppler imaging of the carotid artery. The position of the carotid artery is clearly visible in the ultrasound image (Fig. 3D), with blood flow also demonstrates in the Doppler functional imaging (Fig. 3E). This demonstrates the wide application of the FUT and its potential for ultrasound imaging in other tissues and organs.

To facilitate EMG monitoring, we have developed 10-channel stretchable electrodes by using thermal evaporation of gold on a 2-mm Ecoflex SR layer. Our electrical characterization reveals that these Ecoflex-Au electrodes have remarkable stretchability, reaching up to 650% (Fig. 3F). To facilitate the acquisition of the EMG signal, we use liquid metal as a transitional layer to seamlessly connect the electrodes with the FPCB. We then encapsulate the soft-hard interface with adhesive (DOWSIL 734), confirming a stretchability of 270% (Fig. 3F), which meets the stringent requirements of EMG

monitoring. Furthermore, to reduce the electrodes impedance, we use electroplated Ag/AgCl on the detection pads of Ecoflex-Au electrodes. This modification considerably reduces the Ecoflex-Au electrodes impedance in the low-frequency range when measured in phosphate-buffered saline solution (fig. S21). The contact impedance between the electrodes and the skin drops substantially from 21.52 to 3.63 $k\Omega \cdot cm^2$ at 100 Hz (Fig. 3G). Meanwhile, the electrodes also demonstrate excellent cycling performance. After over 2000 cycles at 100% tensile strain, the resistance changes of the electrodes slightly increase in the first 200 cycles before stabilizing (Fig. 3H). Moreover, more than 100 cycles at 100% strain, the impedance variation of the electrodes remains relatively stable (fig. S22). These findings establish a robust foundation for the reliable monitoring of EMG signals using our electrodes. Our results collectively demonstrate the excellent performance of the FUT and the stretchable Ecoflex-Au electrodes in both muscle ultrasound imaging and EMG monitoring.

Structural-functional dissection by WSFP on normal subjects

The WSFP has an adhesion area of 6 cm by 2.5 cm, with PZT elements measuring 3.8 cm by 0.5 cm, allowing a monitoring depth of ~3 cm. We use an ultrasound coupling agent to prevent the formation of air gaps during imaging. This agent is applied between the PZT array and the skin to maintain continuous contact, thus preventing any disruption in the ultrasound signal caused by air pockets. This method ensures stable imaging throughout dynamic movements. This dual-modal WSFP demonstrates superior performance in the dissection of the structure and function information during activity, outperforming mono-modal monitoring in action classification accuracy. Then, we first use WSFP to monitor the brachioradialis muscle in forearm of normal subjects (Fig. 4, A to C), analyzing ultrasound imaging and EMG data simultaneously during motion. Clear observations from the ultrasound imaging indicate a reduction in muscle thickness and area during fist clenching (Fig. 4, B and C), accompanied by synchronous observation of EMG signals (fig. S23A and movie S4). This reduction in muscle thickness and area correlates with an increase in the RMS of the EMG signal, observed similarly during palm extension (fig. S23B). When the muscle contracts, there is a minor change in muscle size accompanied by an increase in RMS (fig. S24). Furthermore, the structural-functional monitoring under varying gripping forces is assessed (figs. S25 to S28). The accuracy of dual-modal and mono-modal data for action classification is analyzed (Fig. 4D), indicating a favorable recognition accuracy of the dual-modal WSFP.

Subsequently, the effectiveness of the dual-modal WSFP under large deformation is further verified. The erector spinae muscles on the back experience substantial deformation during certain motions, such as stooping down, where the surrounding skin can undergo up to 40% mechanical strain. We then investigate the monitoring capability of WSFP on this muscle (fig. S29 and movie S5). During stooping down, there is a concurrent increase in the RMS of the EMG signal and a synchronous decrease in muscle thickness, both attributed to the muscle contraction (fig. S30). This result is validated during left and right back rotations, as well as left and right flexions (figs. S31 to S34). The dual-modal WSFP achieves continuous synchronous dissection of muscle structure and function during 25% deformations of the erector spinae muscles. Moreover, the WSFP is attached to the mid-belly of the left SCM muscle, parallel to the muscle fibers. As shown in figs. S35 to S39 and movie S6, morphological changes are observed in the ultrasound imaging, accompanied by the successful recording of the generated EMG signals during muscle left and right rotations and flexions.

Leveraging the cyclic stability and long-term wearability of WSFP, we use it for the long-term dissection of muscle structure and function (movie S7). Over a period of 72 hours, the FUT consistently delivers stable imaging capabilities, while the Ecoflex-Au electrodes reliably capture EMG signals during activities such as making fist (Fig. 4E and fig. S40). Over the monitoring period, the quality of ultrasound imaging or EMG signal remains consistently high. Specifically, the muscle thickness and area in ultrasound imaging are consistently detected at 12.82 ± 0.25 mm and 479.12 ± 5.25 mm^2, respectively. The RMS of the EMG signals remains stable at 0.24 ± 0.006 (Fig. 4F). The collection of dual-modal data under various motions, including palm, pinch, index finger pointing, and thumb and index finger pointing consistently yields reliable results, confirming the system's capacity for long-term monitoring with stable performance (figs. S41 to S48). Moreover, the dual-modal data obtained during the long-term monitoring also exhibits higher accuracy in action recognition (Fig. 4G), which is consistent with the results in Fig. 4D, highlighting the substantial potential of WSFP on long-term dissection in disease screening.

Clinical trial of WSFP

Conventional ultrasound imaging is the most commonly used method for diagnosing and evaluating peripheral neuromuscular systems, e.g., CMT, particularly in cases where a palpable mass is present (*9*, *42*). This method primarily identifies structure-related features on the sonogram, such as muscle thickness, echogenicity, and transverse and longitudinal extents (*43*, *44*). However, it lacks the capability to assess muscular functional changes, e.g., leading to the identification failure of the early stage of CMT. Therefore, the development of WSFP capable of simultaneously providing structural and functional features holds promise for enhancing clinical assessments for peripheral neuromuscular system. Here, we assess three CMT patients using WSFP (Fig. 5). EMG mapping in this study reflects the RMS values, indicating muscle activation levels. In patients with CMT, the affected muscles display lower activation during movements, which is represented on the EMG maps as regions with lower intensity. However, the diagnosis of muscle fibrosis is based on ultrasound imaging, where fibrosis manifests as increased muscle thickness and enhanced echogenicity.

We have successfully applied WSFP on SCM muscles of children with CMT to monitor both ultrasound imaging and EMG of different motions. It is found that compared to the healthy side during the four different motion tasks, the affected sides demonstrate sever muscular curvature, blurred edges, muscle fibrosis, and increased muscle thickness from the ultrasound imaging (Fig. 5A). The topographic map based on EMG signals show asymmetry between the two sides of patients with CMT during the motion tasks. For a specific case, the CMT region is located on right side of the child, the EMG topographic maps highlight high-intensity zones indicating muscle activation during different motions. Because of the symmetrical property of the neck muscle, right side with left rotation should be roughly symmetrical to the left side with right rotation for healthy case. However, for the child with CMT, it is quite different and the muscle activation pattern is entirely different (Fig. 5A). For this case, the left top muscle is more likely activated on affected side. While for unaffected side, the activation pattern is relatively random depending on different motions.

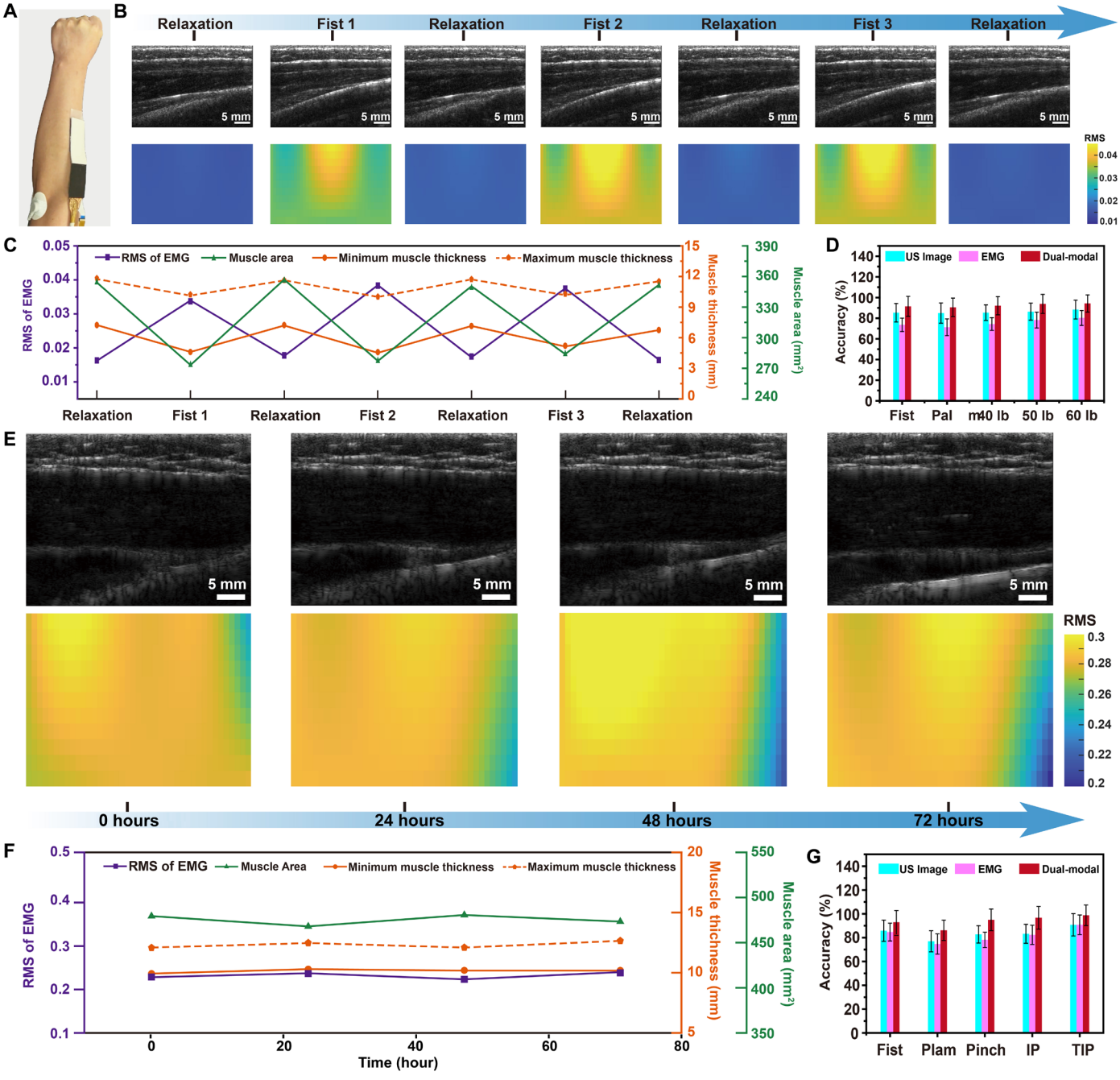

Fig. 4. Dual-modal synchronous monitoring of muscle structure and EMG signals in normal subjects of the forearm brachioradialis muscle. (**A**) Picture of the WSFP attached to the brachioradialis muscle on the forearm for structure-functional monitoring. (**B**) Synchronously acquired ultrasound imaging (i) and EMG maps (ii) of the brachioradialis muscle when relaxation and fist. (**C**) Relative relationship between structural features of muscles (area, minimum, and maximum muscle thickness) and RMS of EMG during synchronized monitoring. (**D**) Accuracy of action recognition for unimodal signals and dual-modal synchronized monitoring signals. (**E**) Synchronously acquired 72-hour wearing and noncontinual dual-modal ultrasound imaging (i) and EMG maps (ii) of palm during the forearm brachioradialis muscle monitoring at initial, 24, 48, and 72 hours. (**F**) Relative relationship between structural features of muscles (area, minimum, and maximum muscle thickness) and RMS of EMG during long-term synchronized monitoring. (**G**) Accuracy of action recognition for unimodal signals and dual-modal synchronized signals of 72 hours. IP, index finger point; TIP, thumb and index finger point.

Furthermore, we compare the ultrasound image parameters and the RMS of EMG from the dual-modal monitoring between the affected and unaffected side (fig. S49). On the affected side, the muscles appear thicker compared to those on the healthy side, and the muscle area is also increased. On the affected side, the brightness of the muscles is notably higher than that on the healthy side due to the increased fibrosis of the affected side. Notably, the abnormal muscle structure on the affected side restricts motions, leading to lower RMS values detected compared to those on the healthy side. To investigate the relationship between the muscle structure and the functional signals generated during muscle activation, we analyze the correlation coefficients between the muscle structural parameters

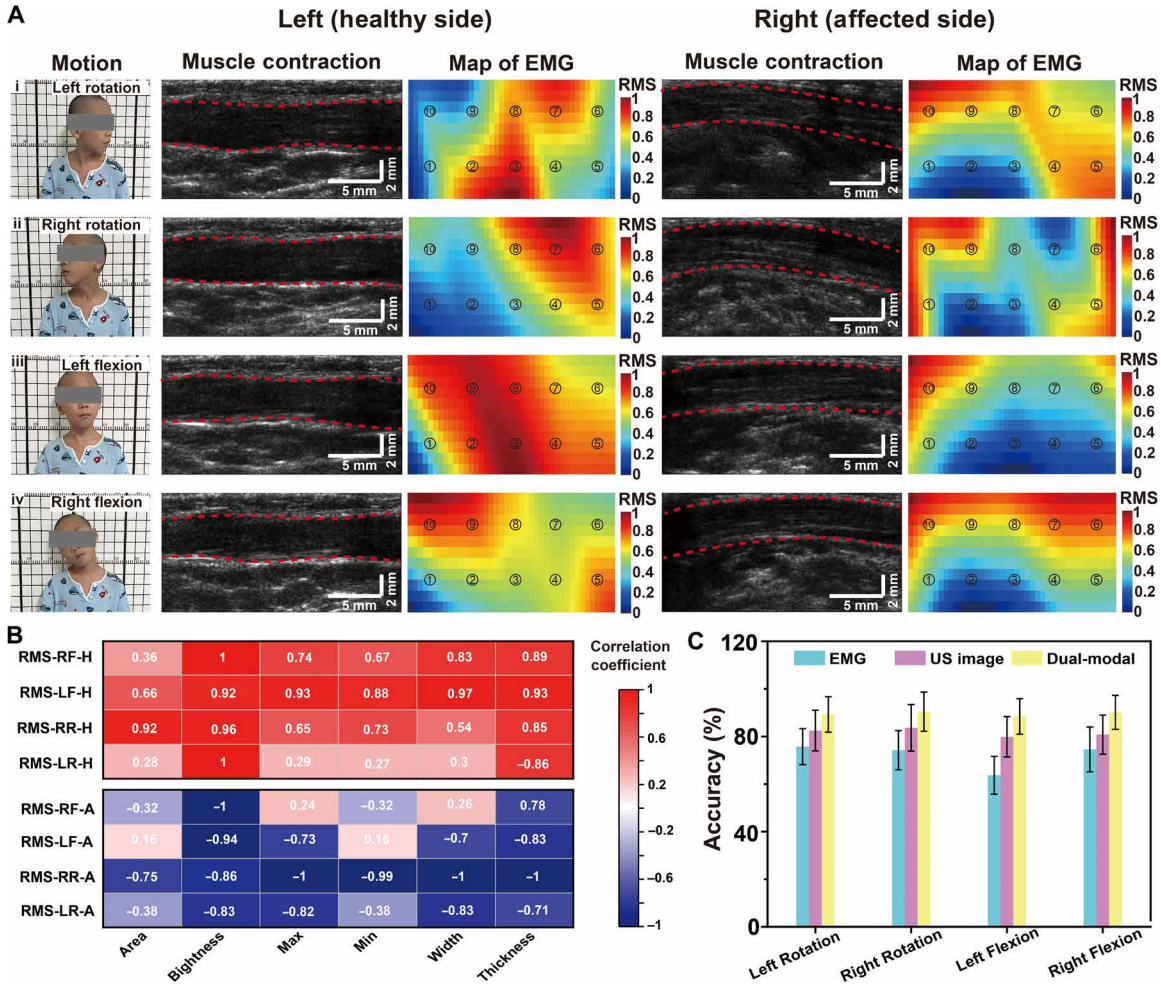

Fig. 5. Structural-functional synchronous monitoring by WSFP on children with CMT. (**A**) Specific case of synchronous ultrasound imaging and EMG monitoring on a child with CMT by WSFP. From top to bottom, the actions are left rotation, right rotation, left flexion, and right flexion, respectively. The area in between the dash read line represents the detected structure of the SCM muscle. Circles represent the electrode positions and sensing areas, with a diameter of 2 mm. Numbers inside indicate the channel number. (**B**) Correlation coefficients among the muscular area, brightness, and size of affected side at rest state, and RMS of EMG during various motions, including left rotation (RMS-LR-H), right rotation (RMS-RR-H), left flexion (RMS-LF-H), and right flexion (RMS-RF-H) on healthy side, as well as left rotation (RMS-LR-A), right rotation (RMS-RR-A), left flexion (RMS-LF-A), and right flexion (RMS-RF-A) on affected side. H represents healthy side, and A represents affected side. (**C**) Accuracy of CMT recognition for unimodal signals and dual-modal synchronized monitoring signals of different actions. US, ultrasound.

from the ultrasound imaging, such as muscular area, brightness, and size, as well as the RMS from EMG on both the affected and unaffected sides (Fig. 5B). During left rotation, RMS exhibits a negative correlation with muscle structural parameters on the affected side, especially with muscle brightness, width, and thickness. This suggests a negative correlation between the degree of muscle damage and the intensity of muscle contraction, which is attributed to the accumulation of noncontractile fibrotic tissue in patients with CMT. As fibrosis progresses, muscle thickness increases, but the number of functional muscle fibers decreases, leading to reduced muscle activation and lower RMS values (*45*, *46*). In other words, the more severe the structural damage, the lower the intensity of muscle contraction. In contrast, during right rotation on healthy side, which exhibits the same muscle activation pattern as left rotation on the affected side, there is a positive correlation between RMS and muscle structural parameters, with muscle brightness and thickness showing a highly positive relationship with RMS. In addition, by separately comparing the correlation between RMS and muscle structural parameters during other motions on the affected and healthy sides, it is found that there is a high correlation between RMS and muscle brightness and thickness, emphasizing a mutual influence between muscle structure and function. EMG mapping in this study reflects the RMS values, indicating muscle activation levels. In patients with CMT, the affected muscles display lower activation during movements, which is represented on the EMG maps as regions with lower intensity. However, the diagnosis of muscle fibrosis is based on ultrasound imaging, where fibrosis manifests as increased muscle thickness and enhanced echogenicity. For example, in Fig. 5A, EMG mapping shows lower intensity in the central region of the affected muscle, while ultrasound imaging reveals

increased thickness and higher echogenicity, both of which are indicative of muscle fibrosis.

Figure 5C illustrates the accuracy of traditional mono-modal ultrasound imaging, EMG signals, and dual-modal signals in classifying CMT across various motions. The selected features for classification include the brightness of ultrasound images and the RMS of EMG. Notably, it can be observed that the mono-modal ultrasound imaging has a higher classification accuracy compared to the mono-modal EMG signals. The classification accuracy of mono-modal ultrasound imaging can exceed 80%, while that of mono-modal EMG is approximately 70%. Specifically, during left flexion, the classification accuracy of mono-modal EMG signals is only 65%. Unexpectedly, when compared with the dual-modal data for CMT disease classification, it is evident that the classification accuracy of dual-modal data exceeds 90% for every motion. Although we have not yet performed a blind test, the combination of functional (EMG) and structural (ultrasound) parameters shows strong potential for distinguishing patients from healthy individuals. Future studies will focus on validating this in blind testing scenarios. These highlights the notable improvement in diagnostic accuracy achieved through the synchronous collection of dual-modal muscle structure and function signals, contributing to a deeper understanding of the disease's pathogenesis.

DISCUSSION

We developed a WSFP for the synchronous dissection of muscle structure and EMG signals, as well as their correlation during motion by integrating a FUT and a stretchable EMG electrode. The FUT exhibits a high frequency and electromechanical coupling coefficient, comparable broadband width to that of the commercial probes, low acoustoelectric crosstalk, as well as excellent stability and durability. The stretchable electrode features 650% stretchability, low impedance, and electrode-skin contact impedance, along with contact cyclic stability. It not only enables the stable EMG signal monitoring, but also serves as a stress-release layer, absorbing the stress generated by skin strain, ensuring the adhesion stability and precise imaging of the FUT even at 40% deformation of skin. The WSFP achieves high-performance and long-term synchronous dissection of dual-modal muscle structure and EMG functional signals in healthy individuals, even during substantial muscle deformation. There is almost no mutual interference between the two signals. In comparison with mono-modal data, dual-modal data exhibit higher accuracy in action recognition. It also realizes dual-modal synchronous dissection of patients with pediatric torticollis, accurately reflecting the differences in the patients' muscle structure and function compared to normal muscles. The dual-modal data demonstrates higher accuracy in disease diagnosis and evaluation during human motion, indicating the wide clinical prospects of the flexible dual-modal sensing system. The potential applicability of WSFP extends beyond healthy individuals and pediatric torticollis patients, offering promising prospects for other neuromuscular conditions, such as amyotrophic lateral sclerosis and stroke-induced neuromuscular impairments. By facilitating simultaneous structural and functional monitoring, WSFP could be used to assess muscle degeneration, motor function decline, and therapeutic efficacy in these populations, further broadening its clinical relevance.

The future advancement of WSFP could be focused on two key aspects. First, optimizing the flexible ultrasound array to make it inherently soft and stretchable would greatly enhance the comfort of wearing the WSFP. However, a critical challenge lies in ensuring high-quality ultrasound imaging under dynamic changes in position of the PZT element. For flexible PZT array, the position of the element is relatively constrained, while for the stretchable one, the distance between elements changes markedly. Overcoming this challenge requires the development of innovative device systems and algorithms to maintain consistent high-quality ultrasound imaging under extreme dynamic conditions. Another aspect is to increase the sensing modalities of WSFP. For structural imaging, optical-based imaging could be integrated further, while for functional monitoring, incorporating biomechanical and bio-acoustic signals (*47*–*50*) would be beneficial. In addition, currently, there is a notable absence of reliable data fusion and processing methods for the simultaneous analysis of structural and functional signals. The stimulation function, e.g., focused ultrasound stimulation array, could be mucked to tune related functions of tissues. It is believed that WSFP would be the next-generation wearable patch for health care and rehabilitation after addressing these challenges.

MATERIALS AND METHODS

Fabrication of the FUT

The FUT was developed by integrating three layers: a flexible acoustic stack, a FPCB, and a flexible backing layer. The flexible acoustic stack was fabricated using a two-step dicing-and-filling method. In the first step, a 2-2 piezocomposite was created by mechanically dicing a piezoelectric ceramic plate (3203HD, CTS Corporation, Bolingbrook, IL, USA) with a high-precision dicing saw (ADT7122, Advanced Dicing Technologies Ltd., Yokneam, Israel). The resulting dicing kerfs were filled with low-viscosity epoxy resin (Epo-Tek 301, Epoxy Technology Inc., Billerica, MA, USA). After polishing to a target thickness of 250 μm, the top and side surfaces were sputtered with Cr/Au electrodes. The first matching layer of alumina powder-loaded epoxy is layered on the top surface, followed by the second matching layer of pure epoxy (face B). In the second step, the bottom surface (face A) of the piezocomposite plate was divided into elements with a spacing of 300 μm, and the kerfs were filled with PDMS (Sylgard 184, Dow Corning Corp., Midland, MI, USA). After repolishing, Cr/Au electrodes were sputtered onto the face A. An isolation cut on face A separated it from the signal electrode, allowing the FPCB to connect to ground and signal electrodes of Face A, with the ground electrode linked to a single ground line on the FPCB. The final thickness of the flexible acoustic stack was measured at 430 μm. To attach the acoustic stack to the FPCB, a custom fixture is used to ensure tight and stable contact. FPCB and acoustic stack are clamped together using this fixture, which provides a secure electrical connection. Once clamped, epoxy resin (Epo-Tek 301, Epoxy Technologies, Billerica, MA, USA) is applied to bond the assembly. This bonding process involves curing at room temperature for 24 hours, followed by an additional 12 hours of curing at 45°C. This method results a robust and stable electrical connection between the FPCB and the acoustic stack. Last, a flexible backing layer composed of alumina powder, hollow glass microspheres, and PDMS was cast onto the backside of the FPCB.

Fabrication of the soft and stretchable electrode

The fabrication of the soft and stretchable electrode involved meticulous steps, integrating materials such as Ecoflex 00-20 and gold and using liquid metal for efficient connectivity to the FPCB. Specifically, a 2-mm–thick Ecoflex 00-20 film, with a mixing ratio of A:B at 1:1,

was chosen as the stretchable substrate. The substrate underwent a preparation process, which included three iterations of spin-coating (200 rpm, 1 min) and subsequent curing at room temperature for 1 hour. A 380-nm–thick layer of gold was then thermally evaporated onto the substrate at an evaporation rate of 10 Å/s, using a patterned mask for precision. To establish the connection between the soft electrode and the FPCB, liquid metal was used. This procedure entailed coating the end of each channel on the stretchable electrode with a layer of liquid metal through mask rolling. Following this, the pins of the FPCB were linked to the liquid metal and secured with an adhesive (DOWSIL 734). To complete the encapsulation process, a thin layer of Ecoflex 00-20 was spin-coated (1300 rpm, 1 min) onto the electrode.

Preparation of WSFP

The SR layer and FUT are integrated using a specially designed double-sided adhesive to ensure secure bonding. Before applying the adhesive, the SR layer undergoes plasma treatment, which enhances surface energy and promotes a stronger and more durable bond between the two layers. To ensure secure adherence of the WSFP to the skin, a surface layer of adhesive was applied to the soft and stretchable electrode using the following procedure. Initially, the electrode's surface underwent plasma treatment, followed by spin coating with a layer of pressure-sensitive adhesive sourced from Desai Chemical Trading Co., Ltd., Jiangyin. Subsequent to curing the pressure-sensitive adhesive at 60°C for 2 hours, the WSFP became ready for use.

Finite element modeling of the SR layer

The tensile forces and deformations of three materials (PDMS, SEBS, and Ecoflex 00-20) adhering to the surface of the skin were calculated using the ABAQUS/standard solver. The skin has dimensions of 100 mm by 40 mm, and the materials have dimensions of 30 mm by 12.5 mm with thicknesses of 0.5 and 2 mm, respectively. Uniaxial displacement loads of 30% in the y direction were applied to both ends of the skin. The unit type used was the eight-node hexahedral hybrid reduced integration unit (C3D8RH).

Characterization of the FUT and the stretchable electrode

Both the electrical and acoustic performance of the FUT were characterized by standard test methods. The electrical impedance of each element was analyzed using an impedance analyzer (6500B, Wayne Kerr Electronics Ltd., London, UK), from which the resonance frequency, and its corresponding impedance and phase angle magnitude could be obtained directly from the electrical impedance/phase spectra.

The acoustic pulse-echo response was measured by exciting individual element using a pulser/receiver (5073PR, Panametrics Inc., Waltham, MA, USA) and receiving the echo signal from its elevated natural focus. The received response was recorded using an oscilloscope (Tektronix MDO34, Tektronix Tech., Beaverton, OR, USA) and analyzed through the fast Fourier transform function for the frequency domain display. The peak-to-peak amplitude of the voltage signal was recorded as sensitivity. The center frequency (f_c) and −6-dB bandwidth (BW) were determined by the lower (f_l) and upper (f_u) frequencies at which the power spectrum was −6 dB less than the maximum value.

The combined electrical and acoustic crosstalk was determined by comparing the transmitted signal on one element and the received signals from the adjacent elements. A function generator was used to excite the element with a sinusoidal tone-burst signal at discrete frequencies (*51*)

$$\text{Crosstalk} = 20\log\left(V_2/V_1\right)$$

where V_1 and V_2 are the peak-to-peak voltages of the excitation signal of one element and the received signal on the adjacent element.

Stretchability and cycle stability of electrode were measured using AG-X Plus 100N universal testing machine (Shimadzu, Japan) equipped with a digital SourceMeter Keithley 2000. Electrochemical impedance spectroscopy measurements were performed using an electrochemical workstation (Chi 760i, Chenhua). Frequency range is 1 to 100,000 Hz.

The measurement of stretchability was conducted using an AG-X Plus 100N universal testing machine (Shimadzu, Japan) equipped with a Keithley 2000 digital multimeter. The measurement is calculated using the formula

$$\text{Stretchability} = \frac{\Delta l}{l_0} \times 100$$

where Δl is the change in length and l_0 is the initial length.

To measure the strain on the skin surface, a line segment was drawn on the target skin area. The initial length of the line (l_0) was recorded. After the skin was stretched, the final length (l) was measured, and the strain was calculated using the formula

$$\text{Strain} = \frac{\left(l - l_0\right)}{l_0} \times 100$$

This method effectively quantifies skin deformation based on the elongation of the line segment during dynamic movements.

Dual-modal synchronous monitoring of the ultrasound imaging and EMG

For the ultrasound imaging, a programmable ultrasound research system (Vantage 256, Verasonics Inc., Kirkland, WA, USA) was used to independently control each channel of the array transducer for signal transmission and reception. For the EMG monitoring, EMG signals were recorded with a biopotential signal recorder (NES-64C01, BS series, SIAT). For the synchronous monitoring of the brachioradialis muscle, the flexible sensing system was attached to the forearm, capturing dual-modal data during normal fist clenching and variations in grip strength. In the case of the erector spinae muscle, the flexible sensing system was affixed to the back to monitor dual-modal data during activities such as bending forward, left and right rotations, and left and right leaning. To monitor the pectoralis major muscle synchronously, the flexible sensing system was attached to the neck, capturing dual-modal data during left and right rotations as well as left and right bending. For long-term synchronous monitoring, the flexible sensing system was adhered to the forearm to record dual-modal data over a 72-hour period. These experiments were conducted on healthy individuals. Although the WSFP remained attached and worn continuously for 72 hours, dual-modal data (ultrasound and EMG) were collected at designated intervals: 0, 24, 48, and 72 hours. These time points were selected to monitor the device's performance over time and to capture any potential variations in muscle structure and function during extended wear while avoiding unnecessary continuous data collection. The experimental protocols were approved by the Institutional Review

Committee of Shenzhen Institutes of Advanced Technology, Chinese Academy of Sciences (SIAT-IRB-220315-H0592).

Clinical application method

This study collected data from three pediatric patients with torticollis for the clinical application of the dual-modal sensing system. The experimental protocols were approved by the Institutional Review Committee of Shenzhen Institutes of Advanced Technology, Chinese Academy of Sciences (SIAT-IRB-220115-H0582). All participants consented to their involvement and the publication of their data/photos for scientific and educational purposes. The dual-modal monitoring method was the same as described previously. The flexible dual-modal sensing system was attached to the normal and diseased sides of the patients' SCM muscles. Synchronous monitoring was conducted during left and right rotations as well as left and right flexion on both the normal and diseased sides to evaluate the performance of the sensing system.

Dual-modal data processing

The software, ImageJ was used to extract muscle structural information from ultrasound images, including measurements of thickness, width, area, maximum and minimum Feret's diameters, and brightness. Muscle thickness was measured manually, and the dimension perpendicular to muscle thickness was defined as muscle width. Area and the maximum and minimum Feret's diameters were calculated directly by manually selecting the muscle region. In addition, the average grayscale value of the selected region was directly computed. The average grayscale value ranged from 0 to 255, where 0 represents black and 255 represents white. Brightness was defined as the average grayscale value divided by 255, with 0 representing black and 1 representing white (*52*).

To process the EMG signals, we applied a band-pass filter within the 20 to 500 Hz range and removed power line interference (50/60 Hz). This approach effectively retained the relevant EMG data while eliminating low-frequency motion artifacts (below 20 Hz).

When recognizing movements, four time-domain features—including wavelength, zero crossing, slope sign change, and mean absolute value—were extracted from EMG signals. Concurrently, the gray-level cooccurrence matrix and appraised eight statistical indices (comprising energy, entropy, contrast, uniformity, anisotropy, correlation, autocorrelation, and variance) were computed on the basis of this matrix from ultrasound images, thereby constituting the features. In addition, in the dual-modal recognition based on EMG and ultrasound images, the support vector machine was selected as the classifier (*53*). The features extracted from signals of two modalities were concatenated and subsequently input into the classifier for recognition. The accuracy is defined as follow

$$\text{Accuracy} = \frac{\text{number of correctly classified samples}}{\text{number of the whole test samples}} \times 100$$

Statistical methods

Correlation analyses were conducted using Correlation Plot of OriginPro 2023. The data represented the averages of three patients.

Supplementary Materials

The PDF file includes:

Figs. S1 to S49
Tables S1 to S3
Legends for movies S1 to S7

Other Supplementary Material for this manuscript includes the following:

Movies S1 to S7

REFERENCES AND NOTES

1. C. Scotton, C. Passarelli, M. Neri, A. Ferlini, Biomarkers in rare neuromuscular diseases. *Exp. Cell Res.* **325**, 44–49 (2014).
2. B. M. Morrison, Neuromuscular diseases. *Semin. Neurol.* **36**, 409–418 (2016).
3. P. Mary, L. Servais, R. Vialle, Neuromuscular diseases: Diagnosis and management. *Orthop. Traumatol. Surg. Res.* **104**, S89–S95 (2018).
4. C. Edmundson, S. J. Bird, Acute manifestations of neuromuscular disease. *Semin. Neurol.* **39**, 115–124 (2019).
5. S. Rangamani, D. Huliyappa, V. Kulothungan, S. Saravanan, P. K. Murugan, R. Mahadevan, C. Rachel Packiaseeli, E. Bobby, K. Sunitha, A. K. Mallick, S. D. Nayak, S. K. Swain, M. Behera, B. K. Nath, A. Swami, A. K. Kalwar, B. Difoesa, V. Sardana, D. Maheshwari, B. Bhushan, D. Mittal, R. N. Chaurasia, L. P. Meena, K. S. Vinay Urs, R. R. Koli, N. Suresh Kumar, P. Mathur, Stroke incidence, mortality, subtypes in rural and urban populations in five geographic areas of India (2018–2019): Results from the National Stroke Registry Programme. *Lancet Reg. Health Southeast Asia* **23**, 100308 (2024).
6. E. L. Feldman, S. A. Goutman, S. Petri, L. Mazzini, M. G. Savelieff, P. J. Shaw, G. Sobue, Amyotrophic lateral sclerosis. *Lancet* **400**, 1363–1380 (2022).
7. T. T. Do, Congenital muscular torticollis: Current concepts and review of treatment. *Curr. Opin. Pediatr.* **18**, 26–29 (2006).
8. E. Leibovitz, The use of fluoroquinolones in children. *Curr. Opin. Pediatr.* **18**, 64–70 (2006).
9. J. C. Y. Cheng, S. P. Tang, T. M. K. Chen, M. W. N. Wong, E. M. C. Wong, The clinical presentation and outcome of treatment of congenital muscular torticollis in infants—A study of 1,086 cases. *J. Pediatr. Surg.* **35**, 1091–1096 (2000).
10. K. Sonmez, Z. Turkyilmaz, B. Demirogullari, I. O. Ozen, R. Karabulut, B. Bagbanci, A. C. Basaklar, N. Kale, Congenital muscular torticollis in children. *ORL J. Otorhinolaryngol. Relat. Spec.* **67**, 344–347 (2005).
11. R. Hosman, F. Cardullo, D. Abbink, The neuromuscular system, in *AIAA Modeling and Simulation Technologies Conference, 8354* (AIAA, Toronto, 2010).
12. H. Zhao, S. Wang, T. Li, Y. Liu, Y. Tang, Z. Zhang, H. Li, Y. Li, X. Li, G. Li, X. Liu, Q. Tian, Z. Liu, Stretchable multi-channel ionotronic electrodes for in situ dual-modal monitoring of muscle-vascular activity. *Adv. Funct. Mater.* **24**, 2308686 (2024).
13. H. Li, F. Han, L. Wang, L. Huang, O. W. Samuel, H. Zhao, R. Xie, P. Wang, Q. Tian, Q. Li, Y. Zhao, M. Yu, J. Sun, R. Yang, X. Zhou, F. Li, G. Li, Y. Lu, P. Guo, Z. Liu, A hybrid strategy-based ultra-narrow stretchable microelectrodes with cell-level resolution. *Adv. Funct. Mater.* **33**, 2300859 (2023).
14. Q. Tian, H. Zhao, X. Wang, Y. Jiang, M. Zhu, H. Yelemulati, R. Xie, Q. Li, R. Su, Z. Cao, N. Jiang, J. Huang, G. Li, S. Chen, X. Chen, Z. Liu, Hairy-skin-adaptive viscoelastic dry electrodes for long-term electrophysiological monitoring. *Adv. Mater.* **35**, e2211236 (2023).
15. L. Zhang, W. Du, J. H. Kim, C. C. Yu, C. Dagdeviren, An emerging era: Conformable ultrasound electronics. *Adv. Mater.* **36**, e2307664 (2024).
16. S. Choi, J. Y. Kim, H. G. Lim, J. W. Baik, Single-element ultrasound imaging system based on mirror scanning, *IEEE International Ultrasonics Symposium (IUS)* (IEEE, 2020).
17. R. Tsumura, D. P. Vang, N. Hata, H. K. Zhang, Ring-arrayed forward-viewing ultrasound imaging system: A feasibility study. *Proc. SPIE Int. Soc. Opt. Eng.* **11319**, 113190K (2020).
18. J. Kim, E. Y. Park, B. Park, W. Choi, K. J. Lee, C. Kim, Towards clinical photoacoustic and ultrasound imaging: Probe improvement and real-time graphical user interface. *Exp. Biol Med. (Maywood)* **245**, 321–329 (2020).
19. L. Zhang, C. Marcus, D. Lin, D. Mejorado, S. J. Schoen, T. T. Pierce, V. Kumar, S. V. Fernandez, D. Hunt, Q. Li, I. I. Shuvo, D. Sadat, W. Du, H. Edenbaum, L. Jin, W. Liu, Y. C. Eldar, F. Li, A. P. Chandrakasan, A. E. Samir, C. Dagdeviren, A conformable phased-array ultrasound patch for bladder volume monitoring. *Nat. Electron.* **7**, 77–90 (2024).
20. H. Hu, H. Huang, M. Li, X. Gao, L. Yin, R. Qi, R. S. Wu, X. Chen, Y. Ma, K. Shi, C. Li, T. M. Maus, B. Huang, C. Lu, M. Lin, S. Zhou, Z. Lou, Y. Gu, Y. Chen, Y. Lei, X. Wang, R. Wang, W. Yue, X. Yang, Y. Bian, J. Mu, G. Park, S. Xiang, S. Cai, P. W. Corey, J. Wang, S. Xu, A wearable cardiac ultrasound imager. *Nature* **613**, 667–675 (2023).
21. M. Lin, Z. Zhang, X. Gao, Y. Bian, R. S. Wu, G. Park, Z. Lou, Z. Zhang, X. Xu, X. Chen, A. Kang, X. Yang, W. Yue, L. Yin, C. Wang, B. Qi, S. Zhou, H. Hu, H. Huang, M. Li, Y. Gu, J. Mu, A. Yang, A. Yaghi, Y. Chen, Y. Lei, C. Lu, R. Wang, J. Wang, S. Xiang, E. B. Kistler, N. Vasconcelos, S. Xu, A fully integrated wearable ultrasound system to monitor deep tissues in moving subjects. *Nat. Biotechnol.* **42**, 448–457 (2023).
22. C. Wang, X. Li, H. Hu, L. Zhang, Z. Huang, M. Lin, Z. Zhang, Z. Yin, B. Huang, H. Gong, S. Bhaskaran, Y. Gu, M. Makihata, Y. Guo, Y. Lei, Y. Chen, C. Wang, Y. Li, T. Zhang, Z. Chen, A. P. Pisano, L. Zhang, Q. Zhou, S. Xu, Monitoring of the central blood pressure waveform via a conformal ultrasonic device. *Nat. Biomed. Eng.* **2**, 687–695 (2018).
23. J. Lv, G. Thangavel, Y. Xin, D. Gao, W. C. Poh, S. Chen, P. S. Lee, Printed sustainable elastomeric conductor for soft electronics. *Nat. Commun.* **14**, 7132 (2023).

24. G. Li, M. Zhang, S. Liu, M. Yuan, J. Wu, M. Yu, L. Teng, Z. Xu, J. Guo, G. Li, Z. Liu, X. Ma, Three-dimensional flexible electronics using solidified liquid metal with regulated plasticity. *Nat. Electron.* **6**, 154–163 (2023).
25. B. Zhang, J. Li, J. Zhou, L. Chow, G. Zhao, Y. Huang, Z. Ma, Q. Zhang, Y. Yang, C. K. Yiu, J. Li, F. Chun, X. Huang, Y. Gao, P. Wu, S. Jia, H. Li, D. Li, Y. Liu, K. Yao, R. Shi, Z. Chen, B. L. Khoo, W. Yang, F. Wang, Z. Zheng, Z. Wang, X. Yu, A three-dimensional liquid diode for soft, integrated permeable electronics. *Nature* **628**, 84–92 (2024).
26. C. Xu, Y. Song, J. R. Sempionatto, S. A. Solomon, Y. Yu, H. Y. Y. Nyein, R. Y. Tay, J. Li, W. Heng, J. Min, A. Lao, T. K. Hsiai, J. A. Sumner, W. Gao, A physicochemical-sensing electronic skin for stress response monitoring. *Nat. Electron.* **7**, 168–179 (2024).
27. Z. Liu, X. Hu, R. Bo, Y. Yang, X. Cheng, W. Pang, Q. Liu, Y. Wang, S. Wang, S. Xu, Z. Shen, Y. Zhang, A three-dimensionally architected electronic skin mimicking human mechanosensation. *Science* **384**, 987–994 (2024).
28. Z. Xiong, S. Zeng, H. Chen, X. Qiu, G. Tang, Y. Tang, S. Tang, Unique finding in congenital muscular torticollis: Clinic screening on the neck of one day old neonate and ultrasonographic imaging from birth through 3 years of follow-up. *Medicine* **98**, e14794 (2019).
29. S. K. Hong, J. W. Song, S. B. Woo, J. M. Kim, T. E. Kim, Z. I. Lee, Clinical usefulness of sonoelastography in infants with congenital Muscular Torticollis. *Ann. Rehabil. Med.* **40**, 28–33 (2016).
30. Y. L. Chan, J. C. Y. Cheng, C. Metreweli, Ultrasonography of congenital muscular torticollis. *Pediatr. Radiol.* **22**, 356–360 (1992).
31. M. Han, L. Chen, K. Aras, C. Liang, X. Chen, H. Zhao, K. Li, N. R. Faye, B. Sun, J. H. Kim, W. Bai, Q. Yang, Y. Ma, W. Lu, E. Song, J. M. Baek, Y. Lee, C. Liu, J. B. Model, G. Yang, R. Ghaffari, Y. Huang, I. R. Efimov, J. A. Rogers, Catheter-integrated soft multilayer electronic arrays for multiplexed sensing and actuation during cardiac surgery. *Nat. Biomed. Eng.* **4**, 997–1009 (2020).
32. T. Li, H. Zhao, H. Li, Z. Zhang, F. Han, P. Fang, G. Li, R. Xie, Q. Li, X. Gao, C. Hu, J. Gong, Z. Liu, Q. Tian, Dual-modal stretchable sensing patches for in situ monitoring of electromyography and acoustic myography. *Adv. Funct. Mater.* 2409780 (2024).
33. H.-S. Choi, EMG sensor system for neck fatigue assessment using rf wireless power transmission, in *Proceedings of the 2018 3rd International Conference on Computational Intelligence and Applications (ICCIA)* (ICCIA, 2018), pp. 219–222.
34. C. Wang, X. Chen, L. Wang, M. Makihata, H.-C. Liu, T. Zhou, X. Zhao, Bioadhesive ultrasound for long-term continuous imaging of diverse organs. *Science* **377**, 517–523 (2022).
35. H.-C. Liu, Y. Zeng, C. Gong, X. Chen, P. Kijanka, J. Zhang, Y. Genyk, H. Tchelepi, C. Wang, Q. Zhou, X. Zhao, Wearable bioadhesive ultrasound shear wave elastography. *Sci. Adv.* **10**, eadk8426 (2024).
36. W. Du, L. Zhang, E. Suh, D. Lin, C. Marcus, L. Ozkan, A. Ahuja, S. Fernandez, I. I. Shuvo, D. Sadat, W. Liu, F. Li, A. P. Chandrakasan, T. Ozmen, C. Dagdeviren, Conformable ultrasound breast patch for deep tissue scanning and imaging. *Sci. Adv.* **9**, eadh5325 (2023).
37. H. M. Heres, M. Sjoerdsma, T. Schoots, M. C. M. Rutten, F. N. van de Vosse, R. G. P. Lopata, Image acquisition stability of fixated musculoskeletal sonography in an exercise setting: A quantitative analysis and comparison with freehand acquisition. *J. Med. Ultrason.* **47**, 47–56 (2020).
38. C. Wang, B. Qi, M. Lin, Z. Zhang, M. Makihata, B. Liu, S. Zhou, Y.-h. Huang, H. Hu, Y. Gu, Y. Chen, Y. Lei, T. Lee, S. Chien, K.-I. Jang, E. B. Kistler, S. Xu, Continuous monitoring of deep-tissue haemodynamics with stretchable ultrasonic phased arrays. *Nat. Biomed. Eng.* **5**, 749–758 (2021).
39. H. Hu, X. Zhu, C. Wang, L. Zhang, X. Li, S. Lee, Z. Huang, R. Chen, Z. Chen, C. Wang, Y. Gu, Y. Chen, Y. Lei, T. Zhang, N. Kim, Y. Guo, Y. Teng, W. Zhou, Y. Li, A. Nomoto, S. Sternini, Q. Zhou, M. Pharr, F. L. di Scalea, S. Xu, Stretchable ultrasonic transducer arrays for three-dimensional imaging on complex surfaces. *Sci. Adv.* **4**, eaar3979 (2018).
40. Q. Huang, J. Lan, X. Li, Robotic arm based automatic ultrasound scanning for three-dimensional imaging. *IEEE Trans. Ind. Electron.* **15**, 1173–1182 (2019).
41. W. Chen, J. Liu, S. Lei, Z. Yang, Q. Zhang, Y. Li, J. Huang, Y. Dong, H. Zheng, D. Wu, T. Ma, Flexible ultrasound transducer with embedded optical shape sensing fiber for biomedical imaging applications. *IEEE. Trans. Biomed. Eng.* **70**, 2841–2851 (2023).
42. L. Lieberman, Y. Dror, Advances in understanding the genetic basis for bone-marrow failure. *Curr. Opin. Pediatr.* **18**, 15–21 (2006).
43. T.-C. Hsu, C.-L. Wang, M.-K. Wang, K.-H. Hsu, F.-T. Tang, H.-T. Chen, Correlation of clinical and ultrasonographic in congenital muscular torticollis. *Arch. Phys. Med. Rehabil.* **80**, 637–641 (1999).
44. J. D. Han, S. H. Kim, S. J. Lee, M. C. Park, S.-Y. Yim, The thickness of the sternocleidomastoid muscle as a prognostic factor for congenital muscular torticollis. *Ann. Rehabil. Med.* **35**, 361–368 (2011).
45. H. X. Chen, S. P. Tang, F. T. Gao, J. L. Xu, X. P. Jiang, J. Cao, G. B. Fu, K. Sun, S. Z. Liu, W. Shi, Fibrosis, adipogenesis, and muscle atrophy in congenital muscular torticollis. *Medicine* **93**, e138 (2014).
46. S. J. Lee, J. D. Han, H. B. Lee, J. H. Hwang, S. Y. Kim, M. C. Park, S. Y. Yim, Comparison of clinical severity of congenital muscular torticollis based on the method of child birth. *Ann. Rehabil. Med.* **35**, 641–647 (2011).
47. W. Yan, G. Noel, G. Loke, E. Meiklejohn, T. Khudiyev, J. Marion, G. Rui, J. Lin, J. Cherston, A. Sahasrabudhe, J. Wilbert, I. Wicaksono, R. W. Hoyt, A. Missakian, L. Zhu, C. Ma, J. Joannopoulos, Y. Fink, Single fibre enables acoustic fabrics via nanometre-scale vibrations. *Nature* **603**, 616–623 (2022).
48. Z. Lin, S. Duan, M. Liu, C. Dang, S. Qian, L. Zhang, H. Wang, W. Yan, M. Zhu, Insights into materials, physics, and applications in flexible and wearable acoustic sensing technology. *Adv. Mater.* **36**, e2306880 (2024).
49. Y. Jiang, S. Ji, J. Sun, J. Huang, Y. Li, G. Zou, T. Salim, C. Wang, W. Li, H. Jin, J. Xu, S. Wang, T. Lei, X. Yan, W. Y. X. Peh, S.-C. Yen, Z. Liu, M. Yu, H. Zhao, Z. Lu, G. Li, H. Gao, Z. Liu, Z. Bao, X. Chen, A universal interface for plug-and-play assembly of stretchable devices. *Nature* **614**, 456–462 (2023).
50. J. Yi, G. Zou, J. Huang, X. Ren, Q. Tian, Q. Yu, P. Wang, Y. Yuan, W. Tang, C. Wang, L. Liang, Z. Cao, Y. Li, M. Yu, Y. Jiang, F. Zhang, X. Yang, W. Li, X. Wang, Y. Luo, X. J. Loh, G. Li, B. Hu, Z. Liu, H. Gao, X. Chen, Water-responsive supercontractile polymer films for bioelectronic interfaces. *Nature* **624**, 295–302 (2023).
51. W. Chen, Q. Zhang, J. Liu, S. Lei, Y. Li, J. Huang, L. Guo, H. Zheng, D. Wu, T. Ma, Design and fabrication of a high-frequency microconvex array transducer for small animals imaging. *IEEE Trans.Ultrason.Ferroelectr. Freq. Control* **69**, 1943–1951 (2022).
52. C. H. Lin, H. C. Hsu, Y. J. Hou, K. H. Chen, S. H. Lai, W. M. Chang, Relationship between sonography of sternocleidomastoid muscle and cervical passive range of motion in infants with congenital muscular torticollis. *Biomed. J.* **41**, 369–375 (2018).
53. X. Peng, Y. Liu, F. Tan, W. Chen, Z. Liu, T. Ma, X. Li, G. Li, A novel transformer-based approach for simultaneous recognition of hand movements and force levels in amputees using flexible ultrasound transducers. *IEEE Trans. Neural Syst. Rehabil. Eng.* **31**, 4580–4590 (2023).

Acknowledgments

Funding: This work was supported by the National Key R&D Program of China (grant nos. 2021YFF0501600 and 2021YFF0501601 to Z.L. and 2020YFA0211400 to T.M.), the National Natural Science Foundation of China (grant nos. 52473269 to Z.L., 62471462 and 62101544 to Q.T., 52450017 and 52202167 to W.Y., 62201558 to F.H., 62201559 to Q.L., and 81927804 to G.L.), the Shenzhen Science and Technology Program (grant no. KQTD20210811090217009 to Z.L.), Shenzhen Key Technology Project (grant nos. JSGGZD20220822095200002 and JSGG20210713091811037 to T.M.), the Shenzhen Peacock Plan (grant no. JSGGKQTD20210831174329010 to T.M.), and the Shenzhen Outstanding Scientific and Technological Innovation Talents (Distinguished Young Scientists,grant no. RCJC20210609104443085 to T.M.). **Author contributions:** H.Z., W.C., and Y. Li conceived the project, designed the experiments, prepared the multimodal wearable patch, and analyzed the data. H.L., T.L., F.H., and J.S. characterized the performance. L.H. and X.P. analyzed simulated data and motion recognition. J.C. prepared the ultrasound transducer. Y.Y. analyzed ultrasound images. X.Q. designed the clinical experiments. Y. Liu, H.Y., W.H., and Q.L. analyzed data of EMG. G.F. and C.Y. assisted in clinical experiments. X. Liu, F.L., X. Li, G.Z., L.W., P.F., G.L., H.Z., and M.Z. provided the suggestions in experiments design and characterization. W.Y., Q.T., T.M., and Z.L. conceived and supervised this work and provided guidance throughout the process. All the authors discussed and commented on the manuscript. **Competing interests:** The authors declare that they are listed as inventors on a patent titled "Manufacturing methods of wearable health monitoring devices and flexible sensors" (patent no. CN114145769B1), issued by the China National Intellectual Property Administration (CNIPA). The inventors include Z.L., T.M., Q.Z., W.C., H.Z., Y. Li, and H.Z. The patent was granted on 21 October 2022, with the serial number CN114145769B1. The publication of this manuscript does not conflict with the patent application or status. The authors declare that they have no other competing interests. **Data and materials availability:** All data needed to evaluate the conclusions in the paper are present in the paper and/or the Supplementary Materials.

Submitted 8 August 2024
Accepted 4 December 2024
Published 8 January 2025
10.1126/sciadv.ads1486